

# On the Simulation of Fragmentation During the Process of Ceramic Tile Impacted by Blunt Projectile with SPH Method in LS-DYNA

Yihua Xiao<sup>1,\*</sup>, Hecheng Wu<sup>1</sup> and Xuecheng Ping<sup>2,\*</sup>

**Abstract:** Ceramics are extensively used in protective structures which are often subjected to projectile impacts. During an impact process of a ceramic target by a projectile, fragmentation occurs in both the target and the projectile. It is challenging to simulate such events and predict residual mass and velocity of the projectile. In this work, we attempt to use smoothed particle hydrodynamics (SPH) in LS-DYNA to reproduce fragmentation of the target and the projectile and predict residual mass and velocity of the projectile during a projectile impact of a ceramic target. SPH models for an alumina ceramic tile impacted by a blunt tungsten heavy alloy projectile are established. SPH simulation results of residual mass and velocity of the projectile as well as ejecta and bulge movements of the ceramic tile are obtained and compared with experimental data and simulation results of other numerical approaches. It is found that SPH simulation can properly reproduce the impact fragmentation of the target and the projectile, and shows advantages over existing numerical approaches in the prediction accuracy of residual mass and velocity. Moreover, effects of some numerical aspects of SPH, including particle spacing, contact treatment and parameters in artificial viscosity and smoothing length, on simulation results are identified. A simple approach using identical smoothing length and balanced artificial viscosity is proposed to reduce particle spacing sensitivity. The observed parametric effects and the proposed approach will provide guidance to set appropriate parameters values for SPH simulation of impact fragmentation.

**Keywords:** Fragmentation, ceramics, simulation, SPH.

## 1 Introduction

Ceramic materials have not only high strength and hardness but also low density. They are often used to construct protective structures such as military vehicle armors and body armors. It is of great significance to investigate dynamic behaviors of ceramic materials under projectile impacts. During the process of a ceramic target impacted by a projectile, shock wave propagates and causes cracks and fragments in the target. The fragments

---

<sup>1</sup> School of Mechatronics and Vehicle Engineering, East China Jiaotong University, Nanchang, China.

<sup>2</sup> College of Mechanical Engineering, Tianjin University of Science and Technology, Tianjin, China.

\*Corresponding Authors: Yihua Xiao. Email: xiaoyihua@ecjtu.edu.cn;

Xuecheng Ping. Email: xcping@tust.edu.cn.

Received: 20 June 2019; Accepted: 05 December 2019.

form ejecta and erode the projectile. Hence, the impact process generally involves fracture and fragmentation of both the target and the projectile.

The performance of ceramic targets subjected to projectile impacts has been studied for a long time [Shockey, Marchand, Skaggs et al. (2018); Anderson and Morris (1992)]. Continuous efforts are made in recent years to deeply investigate fragmentation characteristics and mechanisms of ceramics under impact loading, such as relation between defect distribution and number of fragments [Levy and Molinari (2010)], crack velocity and fragment size distribution [Strassburger, Hunzinger, Parimal et al. (2013); Hogan, Farbaniec, Mallick et al. (2017)] and influences of microstructures [Hogan, Farbaniec, Mallick et al. (2017); Hogan, Farbaniec, Shaeffer et al. (2015); Krell and Strassburger (2014)]. Experiment study plays an important role in the study of impact fragmentation of ceramics and provides much information for understanding fragmentation mechanisms. However, it requires expensive cost and has difficulties in capturing internal features, such as stress propagation and crack initialization and coalescence. Numerical simulation gives an alternative to experiment for studying high velocity impact of ceramics. It has advantages of high efficiency and low cost, and can provide detailed information on stress propagation and fragment formation, which is helpful for understanding fragmentation mechanisms.

Numerical simulation of a ceramic target subjected to a projectile impact is challenging for traditional numerical methods, because both the projectile and the target involve large deformations and fragmentation. Lagrangian finite element method (FEM) with cohesive fracture model [Levy and Molinari (2010); Camacho and Ortiz (1996)] was applied to simulate fragmentation. However, FEM suffers from mesh tangling. It generally requires element erosion to avoid the problem. Due to the removal of elements, element erosion leaves voids at impact interfaces and leads to abrupt interface changes and contact discontinuity, so it is not ideal for modeling formation of fragments and abrasive effects of ceramic fragments on the projectile. Besides the element erosion, converting elements into meshless particles is another method to overcome mesh tangling for FEM. Cottrell et al. [Cottrell, Yu and Owen (2003)] combined this method with element erosion and adaptive remeshing to simulate confined boron carbide ceramic under tungsten projectile impact. In their work, they converted only elements of the ceramic target into undeformable particles. Bresciani et al. [Bresciani, Manes and Romano et al. (2016)] also used the element conversion method to simulate fragmentation of a tungsten heavy alloy projectile penetrating an alumina tile. They converted only elements of the ceramic tile into SPH (smoothed particle hydrodynamics) particles when a failure criterion is satisfied. They modeled the projectile as an assembly of pre-fragmented sub-parts and used a cohesive law to determine separation of the sub-parts. This method requires relatively complex geometrical definition and contact calculation for the projectile and gives poor prediction of residual mass. Besides, it may still suffer from the same problem of conventional FEM since the projectile is modeled with finite elements. To effectively overcome the difficulty of FEM in simulating projectile impact of ceramic target, some researchers used solutions completely depending on meshless methods [Han, Liu, Rajendran et al. (2006)].

SPH [Gingold and Monaghan (1977)] as a meshless Lagrangian particle method is

capable of modeling large deformations. It has been extensively applied to simulate various problems, such as fluid flow [Monaghan (1994)], explosion [Yang, Liu, Hu et al. (2016); Liu, Liu and Zong (2003)], high velocity impact [Zhang and Liu (2017); Xiao and Dong (2017); Rahaman, Pathak and Roy (2018)], heat and mass transfer [Cleary (1998)], material forming [Cleary, Prakash and Ha (2006)], and so on. One can refer to Liu et al. [Liu and Liu (2010)] for a comprehensive understanding of the developments of SPH method and its applications. Due to the truly meshless feature, SPH can easily reproduce material fracture and fragmentation. Some researchers have employed SPH to simulate high velocity impacts of brittle materials [Michel, Chevalier, Durin et al. (2006); Rabczuk and Eibl (2003); Clegg and Hayhurst (1999); Hedayati and Vahedi (2017)]. However, existing studies seldom considered the prediction of morphology and residual mass of fragmented projectile during ballistic impacts of ceramics. Moreover, to model high velocity impacts of solid materials, some numerical aspects of SPH should be given special care. One important aspect is contact treatment. Traditional SPH treats interactions by including particles from different materials in particle approximation. This treatment is valid for fluid flow problems and generally works well for hypervelocity impact problems where materials behave like fluids. However, for ballistic impact problems, it may excite excessive virtual tensile and shear stresses at interfaces and lead to unacceptable results [Johnson and Beissel (1996)]. To overcome this problem, particle-to-particle contact algorithms of SPH were developed [Xiao and Dong (2017); Campbell, Vignjevic and Libersky (2000); Seo and Min (2006); Seo, Min and Lee (2008)]. Some researchers [Xiao and Dong (2017); Seo, Min and Lee (2008)] have used these algorithms in SPH to improve simulation results of high velocity impacts of metal targets, where the targets only exhibit fracture and fragmentation. In simulations of high velocity projectile impacts of ceramic targets, contact treatment of SPH is more difficult, because both projectile and target exhibit fracture and fragmentation, and contact interfaces are rather complex. Currently, effects of contact treatment on simulation of impacts of brittle materials like ceramics are not discussed in literatures. Beside the contact treatment, parameters in SPH, such as coefficients for artificial viscosity and smoothing length, have effects on simulation accuracy, stability and efficiency. Mao et al. [Mao, Liu and Dong (2017)] recently studied the effects of parameters in SPH through a testing example of soil column collapse and gave some guidance to the parameters setting for hydrodynamics problems. Since parameters in SPH are usually problem-dependent, it is also necessary to identify effects of the parameters on the prediction of key features for solid impact problems.

In this work, we aim to examine the ability of SPH in reproducing fragmentation during a projectile impact of a ceramic target and predicting both the residual velocity and the residual mass of the projectile. The SPH solver used here is the one in LS-DYNA [LSTC (2014a, b)]. LS-DYNA is a famous engineering analysis software which originates from DYNA3D developed by Lawrence Livermore National Laboratory in the middle 1970s. It was a finite element-based program in its early development, and began to provide meshfree calculation options including SPH in the early 2000s. LS-DYNA has now become a powerful simulation tool, and has been extensively applied to simulating various complex engineering problems, such as automotive crash, metal forming, explosion, and so on. Based on LS-DYNA, SPH models are established in this work for

an alumina ceramic tile impacted by a blunt tungsten heavy alloy projectile. The models discretize both the projectile and target with SPH particles, so they are easy to establish and free of mesh tangling. The abovementioned two contact methods are used for contact treatment between SPH parts. A comparison between them is performed. Residual mass and velocity of the projectile are predicted, and ejecta and bulge movements of the ceramic tile are reproduced. Simulation results of SPH are compared with experimental results [Nemat-Nasser, Sarva, Isaacs et al. (2002)] to examine the feasibility of SPH method in simulating fragmentation during ceramics impacted by projectiles. The simulation results of SPH are also compared with those obtained from other numerical approaches to show its advantages. Effects of parameters in artificial viscosity and smoothing length on simulation results are studied. Also, particle spacing sensitivity is discussed, and a simple approach is proposed to ease it.

The remainder of this paper is organized as follows. Section 2 introduces the SPH model and constitutive models and parameters used in simulations. Section 3 shows the preliminary SPH simulation results and compares them with experimental results and simulation results of other numerical approaches. Section 4 gives an analysis of parametric effects. Section 5 discusses the particle spacing sensitivity and gives an approach to reduce it. Our main conclusions are drawn in the last section.

## 2 Modeling methodology

### 2.1 Basic principles of SPH method

The SPH method employs a set of scattered particles to represent a problem domain. Based on these particles, particle approximations of field functions and their derivatives are constructed. To obtain the particle approximation of a continuous field function  $u(\mathbf{x})$ , a kernel approximation of the field function is firstly defined as

$$\Pi^h u(\mathbf{x}) = \int_{\Omega} u(\mathbf{x}') W(\mathbf{x} - \mathbf{x}', h) d\mathbf{x}', \quad (1)$$

where  $W$  is the smoothing function which should satisfy a series of conditions (see [Liu and Liu (2003)] for a detailed description), and  $\Omega$  is the non-zero region of the smoothing function which is usually called as support domain or smoothing domain. In SPH, the most commonly used smoothing function is the cubic B-spline function. It is defined as

$$W(\mathbf{x} - \mathbf{x}', h) = \frac{C}{h^d} \times \begin{cases} 1 - \frac{3}{2}\xi^2 + \frac{3\xi^3}{4}, & 0 \leq \xi < 1 \\ \frac{1}{4}(2 - \xi)^3, & 1 \leq \xi < 2 \\ 0, & \xi \geq 2 \end{cases} \quad (2)$$

where  $h$  is the smoothing length,  $C$  is a constant depending on space dimensions,  $d$  is the number of space dimensions,  $\xi = r/h$ , and  $r = |\mathbf{x} - \mathbf{x}'|$  is the distance between points (particles)  $\mathbf{x}$  and  $\mathbf{x}'$ . The kernel approximation in Eq. (1) can be discretized by

replacing the continuous integral over  $\Omega$  with a summation over the neighboring particles of point (particle)  $\mathbf{x}$  (i.e., the particles in  $\Omega$ ). This leads to the particle approximation of the field function. For a particle  $i$  at  $\mathbf{x}_i$ , the particle approximation of the field function is written as

$$\Pi^h u(\mathbf{x}_i) = \sum_{j=1}^N \frac{m_j}{\rho_j} u(\mathbf{x}_j) W(\mathbf{x}_i - \mathbf{x}_j, h), \quad (3)$$

where  $N$  is the number of neighboring particles,  $m$  is the mass, and  $\rho$  is the density. Through a similar procedure, the particle approximation of partial derivatives of the field function  $u(\mathbf{x})$  can be derived as

$$\Pi^h \frac{\partial u(\mathbf{x}_i)}{\partial x^\alpha} = \sum_{j=1}^N \frac{m_j}{\rho_j} u(\mathbf{x}_j) A_{ij}^\alpha, \quad (4)$$

where  $\alpha$  is the space index,  $A_{ij}^\alpha$  is the  $\alpha$ -th component of vector  $\mathbf{A}_{ij}$  which is given by

$$\mathbf{A}_{ij} = \mathbf{A}(\mathbf{x}_i, \mathbf{x}_j) = \frac{\mathbf{x}_i - \mathbf{x}_j}{r_{ij}} \frac{\partial W(\mathbf{x}_i - \mathbf{x}_j, h)}{\partial r_{ij}}, \quad (5)$$

where  $r_{ij} = |\mathbf{x}_i - \mathbf{x}_j|$ .

Impacts between solids are problems involving material strength. Governing equations for them are conservation equations in continuum mechanics. By using Eqs. (3) and (4) to discretize the conservation equations, SPH formulations can be obtained. There are many ways to derive SPH formulation of the governing equations. This gives rise to various versions of SPH equations [Liu and Liu (2003)]. The commonly used SPH equation for conservation of mass is

$$\frac{d\rho(\mathbf{x}_i)}{dt} = \sum_{j=1}^N m_j (v_i^\alpha - v_j^\alpha) A_{ij}^\alpha, \quad (6)$$

where  $t$  is the time. The SPH equation for conservation of momentum can be expressed as [LSTC (2014a)]

$$\frac{dv^\alpha(\mathbf{x}_i)}{dt} = \sum_{j=1}^N m_j \left[ \frac{\sigma^{\alpha\beta}(\mathbf{x}_i)}{\rho_i^2} A_{ij}^\beta - \frac{\sigma^{\alpha\beta}(\mathbf{x}_j)}{\rho_j^2} A_{ji}^\beta \right], \quad (7)$$

where  $v$  is the velocity,  $\sigma$  is the stress, and  $\beta$  is the space index. If the smoothing length is chosen to be symmetric, the favorable symmetric SPH equation for conservation of momentum can be obtained as follows:

$$\frac{dv^\alpha(\mathbf{x}_i)}{dt} = \sum_{j=1}^N m_j \left[ \frac{\sigma^{\alpha\beta}(\mathbf{x}_i)}{\rho_i^2} + \frac{\sigma^{\alpha\beta}(\mathbf{x}_j)}{\rho_j^2} \right] A_{ij}^\beta. \quad (8)$$

## 2.2 SPH model

As shown in Fig. 1, an SPH model for a ceramic tile normally impacted by a blunt projectile is established based on LS-DYNA. The ceramic tile is square and has dimensions of 101.6 mm×101.6 mm×12.7 mm. It is made of 99.5% Al<sub>2</sub>O<sub>3</sub>. The projectile has a diameter of 6.14 mm and a length of 20.86 mm. It is made of tungsten heavy alloy. The impact velocity of the projectile is 903.9 m/s. The configuration of the model corresponds to the experiment performed by Nemat-Nasser et al. [Nemat-Nasser, Sarva, Isaacs et al. (2002)], so our simulation results can be validated by the experimental data presented in the literature.

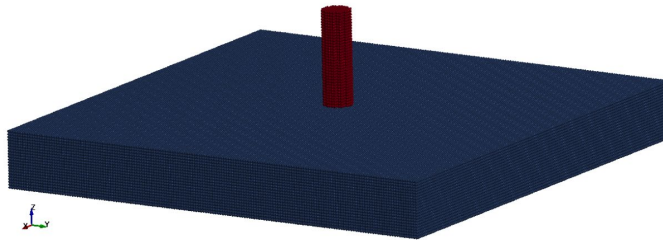


**Figure 1:** SPH model for an Al<sub>2</sub>O<sub>3</sub> ceramic tile normally impacted by a blunt tungsten heavy alloy projectile

In the model, both the projectile and ceramic tile are discretized by uniform SPH particles. By making use of the meshless feature of SPH method, severe deformations and fragmentation of the projectile and ceramic tile can be naturally simulated without the need of special treatments, such as element erosion, adaptive remeshing and use of cohesive elements. The projectile and ceramic tile use the same particle spacing. To analyze the sensitivity of simulation results to particle spacing, different particle spacings detailed below are considered.

In SPH simulation, these are several numerical controls required to be carefully chosen. To keep a relatively stable number of neighboring particles for each particle, smoothing length is allowed to vary in time and space in current simulations. The time integration type for smoothing length is chosen as

$$\frac{dh(t)}{dt} = \frac{1}{d} h(t) \nabla \cdot \mathbf{v} \quad (9)$$

by setting parameter DERIV to 0 in \*CONTROL\_SPH. In our preliminary simulations, the constant applied to smoothing length (the parameter CSLH in \*SECTION\_SPH) is taken as the recommended default value 1.2. In the later analysis of parametric effects, various CSLH values are used to test its effect. Scale factors for the minimum and maximum smoothing lengths (the parameters HMIN and HMAX in \*SECTION\_SPH) are taken as default values 0.2 and 2.0, respectively. The smoothing length of a particle is constrained to the following range

$$HMIN \times h_0 < h(t) < HMAX \times h_0, \quad (10)$$

where  $h_0$  is the initial smoothing length for each part, which is computed in the

initialization stage. The range defined by Eq. (10) is supposed to be sufficiently large for the current problem, because solid materials are nearly incompressible, and particle spacing will not change very significantly before failure of materials, especially for the brittle ceramic material. To avoid numerical oscillation for impact simulation, SPH requires to introduce artificial viscosity. In the current work, the artificial viscosity formulation is chosen as Monaghan type artificial viscosity by defining the parameter IAVIS to 0 in \*CONTROL\_SPH. The formulation of the artificial viscosity is defined as

$$q = \begin{cases} \frac{-Q_2 \bar{c}_{ij} \varphi_{ij} + Q_1 \varphi_{ij}^2}{\bar{\rho}_{ij}}, & v_{ij}^\alpha x_{ij}^\alpha < 0 \\ 0, & v_{ij}^\alpha x_{ij}^\alpha \geq 0 \end{cases}, \quad (11)$$

where

$$\varphi_{ij} = \frac{\bar{h}_{ij} v_{ij}^\alpha x_{ij}^\alpha}{d_{ij}^2 + (0.1 \bar{h}_{ij})^2}, \quad (12)$$

$$v_{ij}^\alpha = v_i^\alpha - v_j^\alpha, \quad x_{ij}^\alpha = x_i^\alpha - x_j^\alpha, \quad (13)$$

$$d_{ij} = \sqrt{x_{ij}^\alpha x_{ij}^\alpha}, \quad (14)$$

$$\bar{c}_{ij} = \frac{1}{2}(c_i + c_j), \quad (15)$$

$$\bar{\rho}_{ij} = \frac{1}{2}(\rho_i + \rho_j), \quad (16)$$

$$\bar{h}_{ij} = \frac{1}{2}(h_i + h_j), \quad (17)$$

where  $c$  is the speed of sound, and  $Q_1$  and  $Q_2$  are the quadratic and linear coefficients, respectively. The two coefficients,  $Q_1$  and  $Q_2$ , depend on problems. They are usually taken as values of order unity for impact problems of solid materials [Zhang and Liu (2017); Xiao and Dong (2017); Rahaman, Pathak and Roy (2018); Seo and Min (2006); Seo, Min and Lee (2008)]. In the preliminary simulations, both  $Q_1$  and  $Q_2$  are set to the recommended default value 1.0. In the later analysis of parametric effects, various combinations of  $Q_1$  and  $Q_2$  with values around 1.0 are used to test their effects.

In addition, treating contacts between the projectile and the ceramic tile is an important issue for SPH simulation of the impact process. Since both the projectile and ceramic tile are represented by particles, it is necessary to treat contacts between SPH parts. This is a challenging task in SPH, because SPH parts lack distinct surfaces. There are two approaches available for contact treatment between SPH parts in LS-DYNA. Both approaches are attempted in this work. The first one is penalty contact method (PCM) which is defined through \*DEFINE\_SPH\_TO\_SPH\_COUPLING. This approach is usually preferred for impact problems where material strength is important, and significant sliding exists on contact interfaces. When this approach is used, computation

of particle approximation between different SPH parts should be turned off by setting the parameter CONT in \*CONTROL\_SPH to 1, and particle approximation is only computed for particles from the same part. For example, for the particle  $i$  of Part B shown in Fig. 2, its particle approximation includes only the effects of particles  $m, n, o, p$  and  $q$  which are within its support domain and from the same Part B. To deal with contacts between different SPH parts, contact is first checked according to the following criterion

$$d_{ij} < SRAD \times \frac{h_i + h_j}{2}, \quad (18)$$

where  $d_{ij}$  is the distance between two particles ( $i$  and  $j$ ) from different SPH parts, and  $SRAD$  is a scale factor. Once contact is detected, penalty forces are applied to contacting particles to prevent their interpenetrations. The penalty force  $F_c$  is calculated as

$$F_c = K_l \delta, \quad (19)$$

where  $K_l$  is the stiffness, and  $\delta$  is the overlap between the contacting particles [Xu and Wang (2014)]. The overlap between contacting particles, for example, particles  $i$  and  $j$  shown in Fig. 2, is calculated as

$$\delta = d_{ij} - SRAD \times (h_i + h_j) / 2, \quad (20)$$

Besides the penalty force, a contact damping force  $F_d$  can be optionally applied to the contacting particles in LS-DYNA. It is calculated as

$$F_d = \eta v, \quad (21)$$

where  $\eta$  is the damping coefficient, and  $v$  is the relative velocity between the contacting particles [Xu and Wang (2014)]. Since  $F_d$  is usually not recommended [LSTC (2014b)], it is not used in the current work by setting the damping coefficient scale factor DFACT as the recommended value 0. The other approach is particle approximation method (PAM). It simply includes particles from different SPH parts in particle approximation to account for contacts, for example, for the particle  $i$  of part B shown in Fig. 2, its particle approximation includes not only the effects of particles  $m, n, o, p$  and  $q$  from Part B but also those of particles  $j, k$  and  $l$  from Part A. This approach is a conventional approach for SPH modeling of fluid interactions, and is also applied to model hypervelocity impact of solids where materials behave like fluids, and material strength is not important. When this approach is used, it is only required to turn on computation of particle approximation between different SPH parts by setting the parameter CONT in \*CONTROL\_SPH to 0. The accuracy of PCM and PAM for the current problem will be compared in the following discussion. For PCM, there are several parameters needed to be set adequately. The penalty scale factor, PFACT, is used to scale the penalty forces ( $F_c$ ). Trial simulations are performed to determine an admissible value of PFACT for the preliminary simulations. A series of values of PFACT are tested in an increasing order, and PFACT is finally determined as 1 which is large enough to prevent significant interpenetrations between the projectile and the ceramic tile and maintain calculation stability. Similarly, the scale factor for contact detection, SRAD, is determined as 1.2 for the preliminary simulations, so that contacts between particles of the projectile and the

ceramic tile can be effectively detected, and non-physical interpenetrations between them can be prevented. This implies contact between two particles from different SPH parts is detected when their distance is less than 1.2 times their average smoothing lengths.

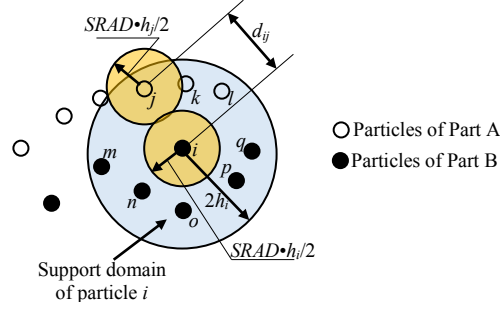


**Figure 2:** Schematic diagram for contact treatment of SPH parts

**2.3 Constitutive models**

*2.3.1 Constitutive model for ceramic material*

JH-2 model [Johnson and Holmquist (1994)] is used to describe material behaviors of Al<sub>2</sub>O<sub>3</sub> ceramic. The model includes pressure, strain rate, damage and bulking effects. It is suitable and popular for modeling high velocity impact of ceramic-type materials. In the model, normalized strength of material is expressed as

$$\sigma^* = \sigma_i^* - D(\sigma_i^* - \sigma_f^*), \tag{22}$$

where  $\sigma^*$  denotes the normalized strength,  $\sigma_i^*$  denotes the normalized intact strength,  $\sigma_f^*$  denotes the normalized fracture strength, and  $D$  is the damage.  $\sigma^*$ ,  $\sigma_i^*$  and  $\sigma_f^*$  are all normalized by the strength at Hugoniot elastic limit (HEL)  $\sigma_{HEL}$ . The normalized intact strength describes the intact material behavior. It is defined as

$$\sigma_i^* = A(P^* + T^*)^N (1 + C \ln \dot{\epsilon}^*). \tag{23}$$

The normalized fracture strength describes the damaged material behavior. It is given as

$$\sigma_f^* = B(P^*)^M (1 + C \ln \dot{\epsilon}^*) \leq SFMAX. \tag{24}$$

In Eqs. (23) and (24),  $A$ ,  $B$ ,  $C$ ,  $M$  and  $N$  are constants,  $P^* = P/P_{HEL}$  is the normalized pressure, where  $P$  and  $P_{HEL}$  are the actual pressure and pressure at the HEL, respectively,  $T^* = T/P_{HEL}$  is the normalized maximum tensile pressure, where  $T$  is the maximum tensile pressure that the material can undergo,  $\dot{\epsilon}^* = \dot{\epsilon}/\dot{\epsilon}_0$  is the dimensionless strain rate, where  $\dot{\epsilon}$  and  $\dot{\epsilon}_0$  are the actual strain rate and the reference strain rate, respectively, and the optional parameter SFMAX is used to limit normalized fracture strength. The damage  $D$  is accumulated with the following rule

$$D = \sum \Delta \varepsilon^P / \varepsilon_f^P, \quad (25)$$

where  $\Delta \varepsilon^P$  is the increase of plastic strain during a computational cycle, and the plastic strain to fracture  $\varepsilon_f^P$  is defined as

$$\varepsilon_f^P = D_1 (P^* + T^*)^{D_2}, \quad (26)$$

where  $D_1$  and  $D_2$  are constants.

In the model, the pressure for intact material is calculated by

$$P = \begin{cases} K_1 \mu + K_2 \mu^2 + K_3 \mu^3, & \mu \geq 0 \\ K_1 \mu, & \mu < 0 \end{cases}, \quad (27)$$

where  $K_1$ ,  $K_2$  and  $K_3$  are constants, and  $\mu = \rho / \rho_0 - 1$  where  $\rho$  and  $\rho_0$  are the current and initial density, respectively. The pressure for damaged material in compression is calculated as

$$P = K_1 \mu + K_2 \mu^2 + K_3 \mu^3 + \Delta P, \quad (28)$$

where  $\Delta P$  is determined by converting a part of elastic energy loss to potential hydrostatic energy. The fraction of elastic energy loss converted to potential hydrostatic energy is defined as  $\beta$  ( $0 \leq \beta \leq 1$ ).

**Table 1:** JH-2 model constants for ceramic tile [Cronin, Bui, Kaufmann et al. (2003)]

Strength constants								
<i>A</i>	<i>B</i>	<i>C</i>	<i>M</i>	<i>N</i>	<i>HEL</i> (GPa)	<i>EPSI</i>	<i>T</i> (GPa)	<i>PHL</i> (GPa)
0.93	0.31	0.0	0.6	0.6	2.79	1.0	0.2	1.46
Damage constants			Equation of state				Density	Shear modulus
<i>D</i> <sub>1</sub>	<i>D</i> <sub>2</sub>	<i>K</i> <sub>1</sub> (GPa)	<i>K</i> <sub>2</sub> (GPa)	<i>K</i> <sub>3</sub> (GPa)	$\beta$	$\rho$ (kg/m <sup>3</sup> )	<i>G</i> (GPa)	
0.005	1.0	130.95	0.0	0.0	1.0	3921	90.16	

The material type 110 defining the JH-2 model is used for the ceramic tile. The JH-2 model constants for 99.5% Al<sub>2</sub>O<sub>3</sub> ceramic have been reported by Cronin et al. [Cronin, Bui and Kaufmann et al. (2003)]. The same constants are employed in this work except for the density which is slightly modified to exactly match the actual density of 99.5% Al<sub>2</sub>O<sub>3</sub> ceramic tile used in the experiment [Nemat-Nasser, Sarva, Isaacs et al. (2002)]. The material constants for the ceramic tile are listed in Tab. 1.

### 2.3.2 Constitutive model for projectile material

The projectile material is modeled with Johnson-Cook model and Grüneisen equation of state (EOS). The yield strength in Johnson-Cook model is calculated as

$$\sigma = \left[ A' + B' (\varepsilon^P)^n \right] (1 + C' \ln \varepsilon^*) (1 - T^{*m}), \quad (29)$$

where  $A'$ ,  $B'$ ,  $C'$ ,  $n$  and  $m$  are material constants,  $\varepsilon^P$  denotes the equivalent

plastic strain;  $\dot{\epsilon}^* = \dot{\epsilon}/\dot{\epsilon}_0$  where  $\dot{\epsilon}$  and  $\dot{\epsilon}_0$  are the strain rate and the reference strain rate, respectively;  $T^* = (T - T_r)/(T_m - T_r)$  where  $T$  is the current temperature,  $T_r$  is the room temperature, and  $T_m$  is the melting temperature. The pressure is calculated by Grüneisen EOS with cubic shock velocity ( $U_s$ )-particle velocity ( $U_p$ ), which is defined as

$$P = \frac{\rho_0 c_0^2 \mu \left[ 1 + \left( 1 - \frac{\gamma_0}{2} \right) \mu - \frac{a}{2} \mu^2 \right]}{\left[ 1 - (S_1 - 1) \mu - S_2 \frac{\mu^2}{\mu + 1} - S_3 \frac{\mu^3}{(\mu + 1)^2} \right]^2} + (\gamma_0 + a \mu) E \quad (30)$$

for compressed material and as

$$P = \rho_0 c_0^2 \mu + (\gamma_0 + a \mu) E \quad (31)$$

for expanding material, where  $S_1$ ,  $S_2$  and  $S_3$  are coefficients of the slope of  $U_s - U_p$  curve,  $\gamma_0$  is Grüneisen coefficient, and  $a$  is the first order volume correction to  $\gamma_0$ . Damage of material is defined as

$$D = \sum \Delta \epsilon_p / \epsilon^f, \quad (32)$$

where  $\Delta \epsilon_p$  is the effective plastic strain during an integration cycle, and the strain at failure is given by

$$\epsilon^f = \max \left( \left[ D_1 + D_2 \exp(D_3 \sigma^*) \right] (1 + D_4 \ln \epsilon^*) (1 + D_5 T^*), \epsilon_{\min}^f \right), \quad (33)$$

where  $D_1$ ,  $D_2$ ,  $D_3$ ,  $D_4$  and  $D_5$  are damage constants,  $\epsilon_{\min}^f$  is the minimum failure strain, and  $\sigma^*$  is the ratio of mean stress  $\sigma_m$  ( $\sigma_m = -P$ ) to effective stress  $\sigma_{\text{eff}}$ , i.e.,

$$\sigma^* = \sigma_m / \sigma_{\text{eff}}. \quad (34)$$

The density of projectile material is calculated according to the actual projectile mass and geometric dimensions used in the experiment [Nemat-Nasser, Sarva, Isaacs et al. (2002)]. The material constants for the projectile material used in calculations are listed in Tab. 2.

**Table 2:** Model constants for projectile material [Holmquist, Templeton and Bishnoi (2001)]

Shear modulus		Johnson-Cook strength model constants			
$G$ (GPa)	$A'$ (MPa)	$B'$ (MPa)	$C'$	$n$	$m$
124	1200	141	0.016	0.12	1.0
Johnson-Cook fracture model constants					Density
$D_1$	$D_2$	$D_3$	$D_4$	$D_5$	$\rho$ (kg/m <sup>3</sup> )
0.0	0.33	-1.50	0.0	0.0	17162
Grüneisen EOS					
$c_0$ (m/s)	$S_1$	$S_2$	$S_3$	Grüneisen coefficient $\gamma_0$	
4029	1.23	0.0	0.0	1.54	

### **3 Simulation results and discussions**

This section presents results of our preliminary simulations, which take parameters in SPH as the values mentioned in Section 2.2. The simulation results are compared with experimental results to examine the feasibility and accuracy of SPH for predicting fragmentation of the projectile and the target during the impact process. Also, a comparison of simulation results of SPH using different contact treatments as well as other numerical approaches is performed.

#### ***3.1 Residual velocity and mass of projectile***

First, residual velocity and mass of the projectile are quantitatively analyzed. To determine the residual velocity and mass of the projectile for SPH simulations, the following methods are employed. The residual velocity of the projectile is taken as the resultant rigid body velocity of the SPH part of the projectile. The residual mass of the projectile is calculated as the initial projectile mass minus the mass of fully damaged projectile particles. The fully damaged part of the projectile cannot undergo any stress. It will be easily stripped from the remaining part of the projectile during the recover process of residual projectile, so it is reasonable to remove the weight of the fully damaged part of the projectile from its residual mass. Fig. 3 gives an example for the residual mass prediction. A whole simulated projectile after impact is shown with its damage contour in Fig. 3(a). To predict the residual mass of the projectile, a damage limit is specified to exclude severely damaged particles. In our practical calculation, the damage limit is taken as 0.99, which means only those nearly fully damaged projectile particles are removed. Fig. 3(b) shows the projectile after removing particles whose damage exceeds the limit. The mass of remained projectile particles shown in Fig. 3(b) are calculated and considered as the residual mass of the projectiles. The residual mass is found to be insensitive to the damage limit. It shows a variation within 1% when the damage limit changes from 0.99 to 0.85. The foregoing residual mass prediction method is expected to somewhat overestimate the residual mass due to the following two reasons. One is that isolated particles or particle groups (see Fig. 3(b)) exist after removing damaged particles, and they are counted in the residual mass though they should not be a part of the residual projectile. The isolated particles or particle groups are not totally damaged, because: their surrounding particles damage faster than themselves, and they do not undergo loads from the projectile after their surrounding particles become totally damaged; also, these particles do not contact the target particles and undergo loads from the target. The other one is that particles close to complete damage may be also eroded from the residual projectile during the recover process of residual projectile.

Four particle spacings including 0.8 mm, 0.6 mm, 0.4 mm and 0.3 mm are used in our SPH simulations to examine particle spacing sensitivity. The total numbers of particles for the four spacings are 259,416, 602,581, 2,073,716 and 4,848,802, respectively. The minimum particle spacing is limited to 0.3 mm, due to the significantly increased computational time and limitation of computational capability when using a particle spacing of 0.2 mm or a smaller value.

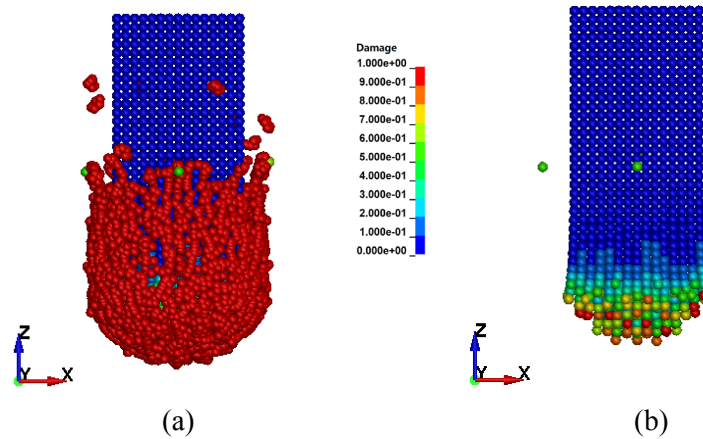


**Figure 3:** Residual mass prediction: (a) Simulated whole projectile; (b) Projectile after removing damaged particles

Tab. 3 gives the results of residual velocity and mass of the projectile obtained by different approaches. The simulation results of SPH show some sensitivity to particle spacing. When PCM is used for contact treatment, the calculated residual velocity and mass exhibit variations of 8.5% and 11.1%, respectively, with respect to corresponding experiment values. When PAM is used for contact treatment, variations of the calculated residual velocity and mass are 7.6% and 14.5%, respectively. The calculated residual velocity and mass tend to continuously increase with the decrease of particle spacing. This is consistent with the observation in FEM simulations of impact-induced plugging failure [Kane, Børvik, Hopperstad et al. (2009)]. The mesh sensitivity in FEM simulations is supposed to be mainly the consequence of strain localization induced by strain softening [Pijaudier-Cabot, ASCE, Bažant et al. (1987)]. The same mechanism can be used to explain the particle spacing sensitivity in SPH simulations. Strain-based damage models are used for materials of both the projectile and the target. When strain increases, damage accumulates, and material degradation occurs. This strain softening effect makes strain and damage localize in a decreasing volume as the particle discretization is refined. When the particle discretization is refined to a vanishing size, the damage volume tends to a vanishing volume, and the projectile and the target tend to fail at zero energy dissipation. In FEM simulations of fracture problems, the nonlocal method is usually used to reduce the mesh sensitivity [Kane, Børvik, Hopperstad et al. (2009); Pijaudier-Cabot, ASCE, Bažant et al. (1987)]. It averages history variables in constitutive models over a domain. The size of the averaging domain is a key parameter and usually a characteristic of material. In SPH, the nonlocal effect is inherent in the sense of particle approximation. SPH employs particle approximation to calculate history variables involved in constitutive models. The particle approximation is defined over a smoothing domain and has an averaging effect. When strain rate at a particle is calculated with the particle approximation, the calculation is related to not only the particle itself but also all other particles in its smoothing domain. Thus, the calculated strain rate is nonlocal, and so are the resultant variables, such as strain, stress and damage. The size of the smoothing domain is proportional to both the parameter CSLH and particle spacing.

In the above particle spacing sensitivity test, CSLH is fixed, so the smoothing domain continuously decreases with the reduction of particle spacing. Consequently, nonlocal effect decreases, and localization of strain and damage becomes more severe. Since more localized damage leads to less damaged regions of the projectile and less resistance of the target, the calculated residual mass of the projectile increases, while its residual velocity increases. Hence, a certain particle spacing sensitivity is observed, though the nonlocal effect has been introduced. Based on the above analysis, keeping identical smoothing domain is expected to be helpful for reducing the particle spacing sensitivity. This point will be discussed later in the paper. Besides the consideration of nonlocal effect, improving computational accuracy and convergence of SPH for field variables may also benefit to reduction of the particle spacing sensitivity, since this can reduce differences between computational results of stress and strain fields for different particle spacings. To achieve this, using corrective techniques to restore consistency of SPH particle approximation is an effective way. However, corrective techniques, such as modified smoothed particle hydrodynamics (MSPH) [Zhang and Batra (2004)], symmetric smoothed particle hydrodynamics [Zhang and Batra (2009); Song, Xing, Hou et al. (2018)] (SSPH) and finite particle method (FPM) [Liu, Xie and Liu (2005)], generally require inversion of coefficient matrices. This brings problems in numerical stability and robustness for fragmentation simulations, because isolated particles and particles forming small fragments are inevitably generated during a fragmentation process, and their coefficient matrices are singular due to the lack of enough neighboring particles. The effect of corrective techniques in reducing the particle spacing sensitivity will be investigated in future studies.

From the perspective of accuracy, absolute values of relative errors between the simulated and experimental residual velocities are within 9% and 7%, respectively, for SPH simulations with PCM and PAM. This indicates that SPH achieves a good prediction of residual velocity when using particle spacing between 0.3 mm to 0.8 mm. The prediction accuracy of residual velocity of SPH is comparable to that of the fragmentation method [Bresciani, Manes, Romano et al. (2016)], while is higher than that of the erosion method based on FEM [Bresciani, Manes, Romano et al. (2016)]. SPH overestimates the residual mass of the projectile. Maximum absolute values of relative errors between the simulated and experimental residual masses are about 20% and 18%, respectively. SPH simulation with PAM gives a slightly better prediction accuracy of residual mass than SPH simulation with PCM. In general, the prediction accuracy of residual mass of SPH is acceptable. Compared with the fragmentation method and erosion method, SPH achieves a much better prediction accuracy of residual mass.

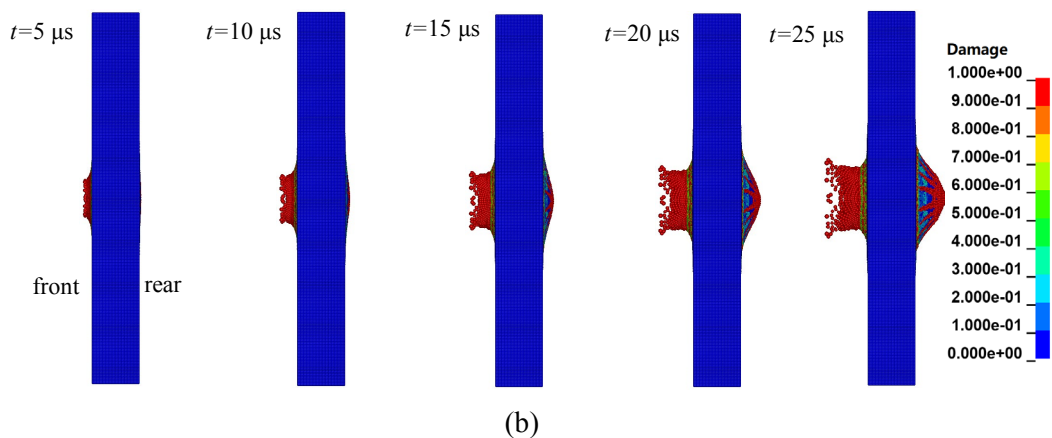
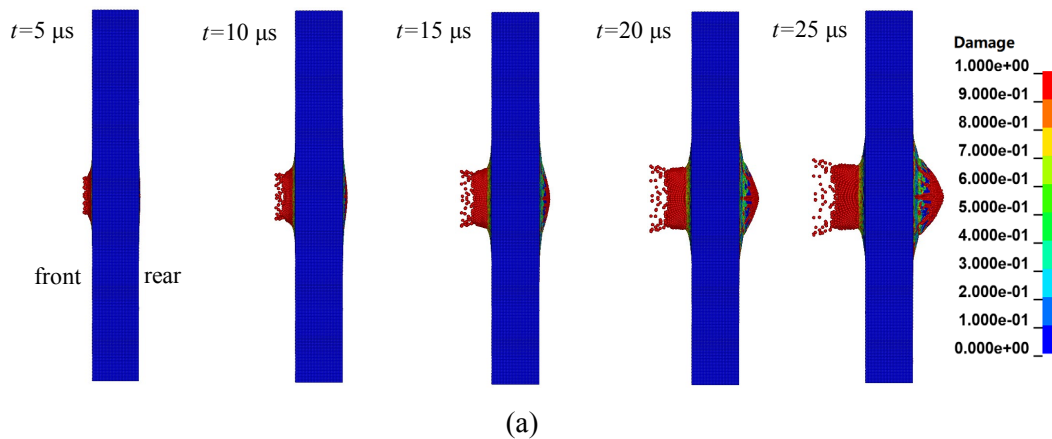
**Table 3:** Comparison of results obtained by different approaches

Simulation method		Particle spacing for SPH and element size for fragmentation method (mm)		Residual velocity (m/s)/relative error	Residual mass (g)/relative error	
SPH with PCM		0.8		680/-0.3%	7.01/9.2%	
		0.6		700/2.6%	7.39/15.1%	
		0.4		727/6.6%	7.51/17.0%	
		0.3		738/8.2%	7.72/20.2%	
SPH with PAM		0.8		676/-0.9%	6.65/3.6%	
		0.6		692/1.5%	7.23/12.6%	
		0.4		715/4.8%	7.27/13.2%	
		0.3		728/6.7%	7.58/18.1%	
Fragmentation method	Sector number	Sector size	Target	Projectile		
[Bresciani, Manes, Romano et al. (2016)]	3	about 1.0	0.4	an average of 0.1	600/-12.0%	3/-53.3%
using different radial sectors	5	about 0.6			675/-1.0%	4.28/-33.3%
	7	about 0.4			683/0.0%	3.85/-40.0%
Erosion method [Bresciani, Manes, Romano et al. (2016)]				-	782/14.7%	10.6/65.1%
Experiment method [Nemat-Nasser, Sarva, Isaacs et al. (2002)]				-	682.0	6.42

**3.2 Deformation and fragmentation of target**

Then deformation and fragmentation of the target during the impact process are analyzed. Since the simulated deformation and fragmentation modes for different particle spacings are similar, simulated results with particle spacing 0.4 mm are only detailedly shown in Fig. 4 to illustrate the deformation process of the target. Fig. 4(a) shows the result obtained by SPH with PCM. As seen from the figure, ceramic ejecta is ejected from the front face soon after impact. The materials in the ejecta are totally damaged. This implies that the ejecta is pulverized. The ejecta becomes radically disperse and gradually forms a conical shape as the impact progresses. This ejection process brings away the pulverized ceramic in front of the projectile and benefits to the penetration of the projectile into the ceramic target. At the rear face of the target, displacements are obviously observed at the time of about 10 μs after impact, and a rounded bulge is formed. The bulge expands towards the motion direction of the projectile. Fig. 4(b) gives the simulated results for

SPH with PAM. Similar pulverized ejecta and rounded bulge are observed at the front face and the rear face, respectively. Nemat-Nasser et al. [Nemat-Nasser, Sarva and Isaacs et al. (2002)] used high speed photography to record the deformation process of the target. The high-speed photographs clearly showing back face displacement and bulge are included here and given in Fig. 4(d). It can be seen from the figure that a large amount of sabot debris is created at the front face during the sabot stripping process and interferes with the observation of ceramic ejecta. To avoid the problem, an unstripped-sabot test was also performed by Nemat-Nasser et al. This produced clear photographs of the initial stage of ceramic ejection process at the front face. The photograph showing ceramic ejecta at the time of  $5 \mu\text{s}$  is included here and given in Fig. 4(c). Comparing the simulated images and photographs from experiments, we can conclude that the simulated shapes of ejecta at the front face and bulge at the back face are qualitatively in good agreement with experimental ones. Fig. 5 shows simulated deformations of the target at  $10 \mu\text{s}$  after impact for different particle spacings. The deformation modes are similar. The back faces are all just slightly displaced. According to the high-speed photograph for the same time (i.e. the leftmost image in Fig. 4(d)), we may conclude that the simulated back face displacements seem to agree well with the experimental one.



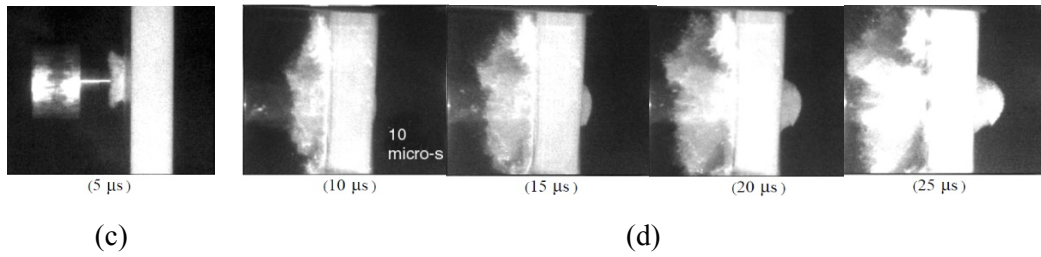


**Figure 4:** Simulation results of deformation process of the target: (a) SPH with PCM; (b) SPH with PAM; (c) Experiment observation of ceramic ejecta in the initial stage of impact [Nemat-Nasser, Sarva, Isaacs et al. (2002)]; (d) Experiment observations of back face displacement and bulge [Nemat-Nasser, Sarva, Isaacs et al. (2002)]. Reproduced with permission from “Nemat-Nasser et al. (2002): Novel ideas in multi-functional ceramic design. Ceramic Transactions, vol. 134, pp. 511-525”. Copyright 2002, The American Ceramic Society.

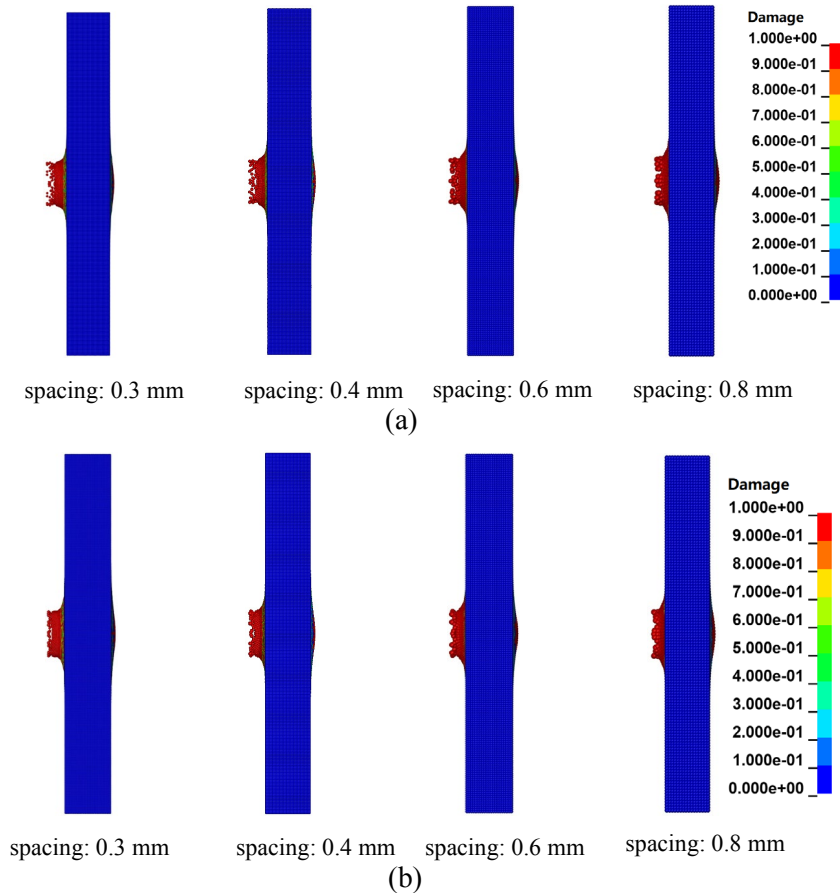


**Figure 5:** Simulated deformations of the target at 10  $\mu$ s after impact using different particle spacings: (a) SPH with PCM; (b) SPH with PAM

Fig. 6 shows the damage pattern of the target which is simulated by SPH with PCM. From the front view and back view of the target, radial and circular damage bands (cracks) are observed. The radial damage bands in bright red indicates cracks have extended to the front face and back face. The ones in dark red indicates cracks are still embedded in the target. From the section view of the target, it can be seen that conical damage zones are formed near the front face and back face.

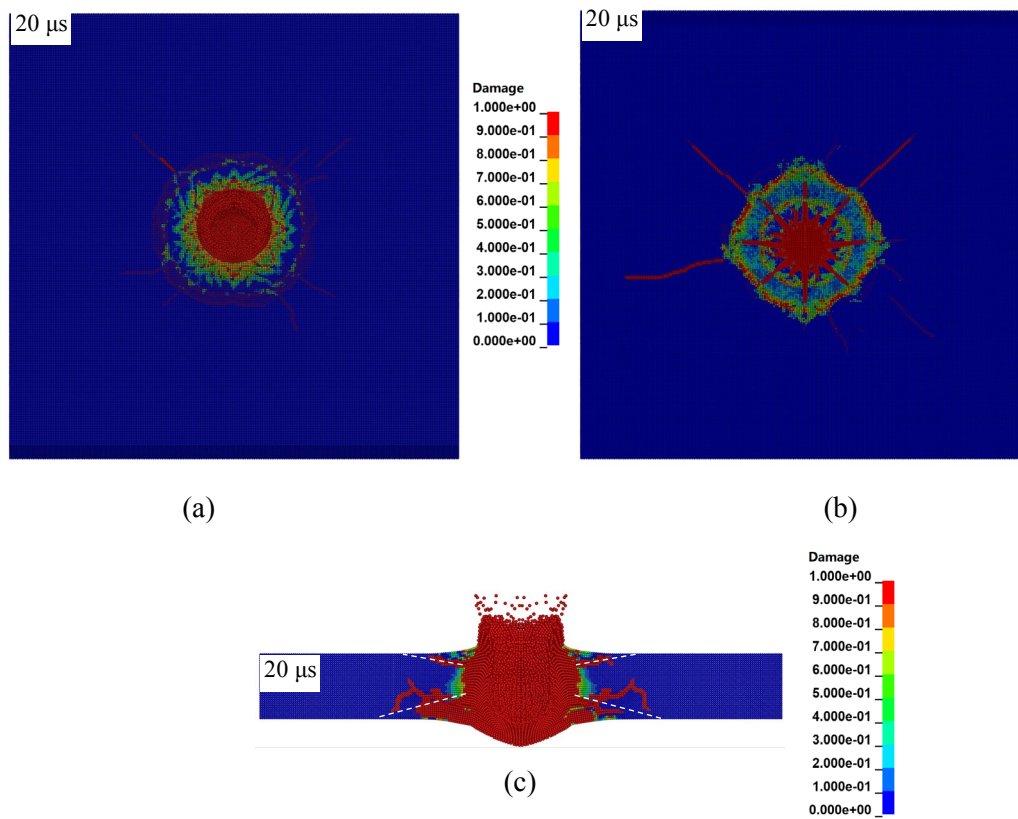


**Figure 6:** Damage contour of the target: (a) Front view; (b) Back view; (c) Section view

### 3.3 Deformation and fragmentation of projectile

Deformation and fragmentation of the projectile during the impact process are finally analyzed. Fig. 7(a) shows the simulated deformation process of the projectile for SPH with PCM using particle spacing of 0.4 mm. It can be seen that mushrooming deformation of the projectile is well reproduced. The projectile mainly deforms at its tip with a mushrooming deformation to form a mushroom head. The mushroom head of the projectile grows in radial size before about 10 μs due to resistance from the ceramic target. Projectile materials near the surface of the mushroom head are fully damaged and lose material strength. They are sheared to flow to the tail of the projectile. With the damaged materials flow away from the head, new materials at the projectile head come out and contact with the target, then they are damaged and flow away again. Such a process repeats, so the projectile is eroded continuously. Fig. 7(b) gives the simulated

results for SPH with PAM. Similar mushroom head of the projectile are reproduced. Fig. 8 shows simulated deformations of the projectile at 8  $\mu$ s after impact for different particle spacings. Less mushrooming deformation is observed with the increase of particle spacing. Nemat-Nasser et al. [Nemat-Nasser, Sarva and Isaacs et al. (2002)] used flash radiography to capture the deformation of the projectile during penetration process. The X-ray image of the projectile for 8  $\mu$ s after impact can be found in Fig. 8 of Nemat-Nasser et al. [Nemat-Nasser, Sarva, Isaacs et al. (2002)]. According to that X-ray image, we can see that the simulated mushrooming deformation of projectile using a smaller particle spacing seems to achieve a better prediction.

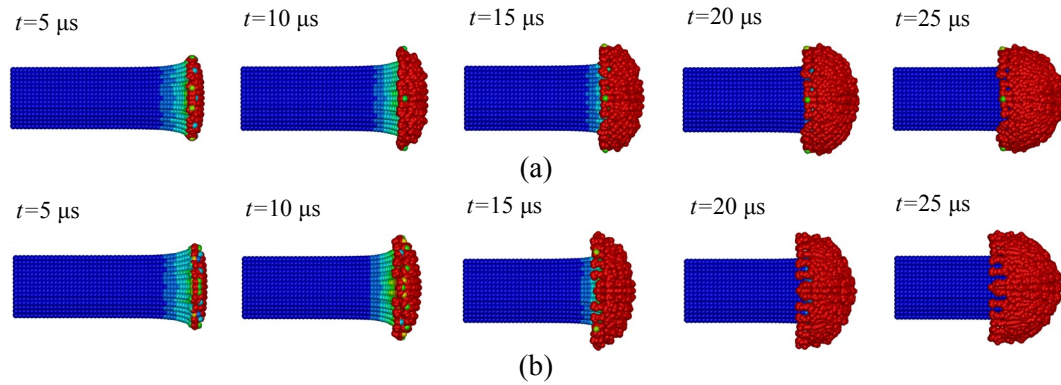


**Figure 7:** Simulation results of deformation process of the projectile: (a) SPH with PCM; (b) SPH with PAM

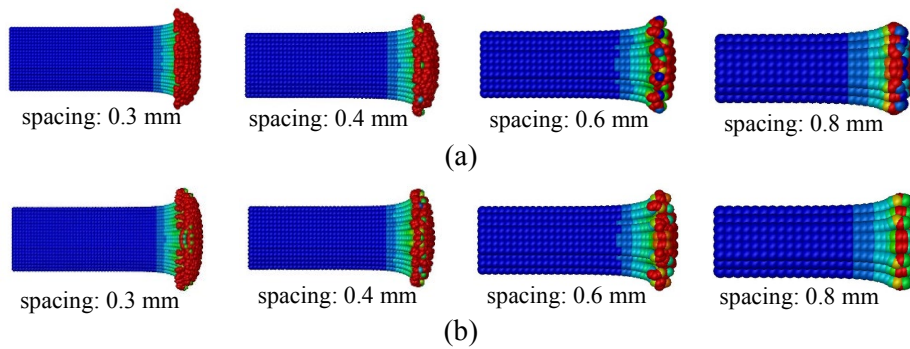


**Figure 8:** Simulated deformations of the projectile at 8  $\mu$ s after impact using different particle spacings: (a) SPH with PCM; (b) SPH with PAM

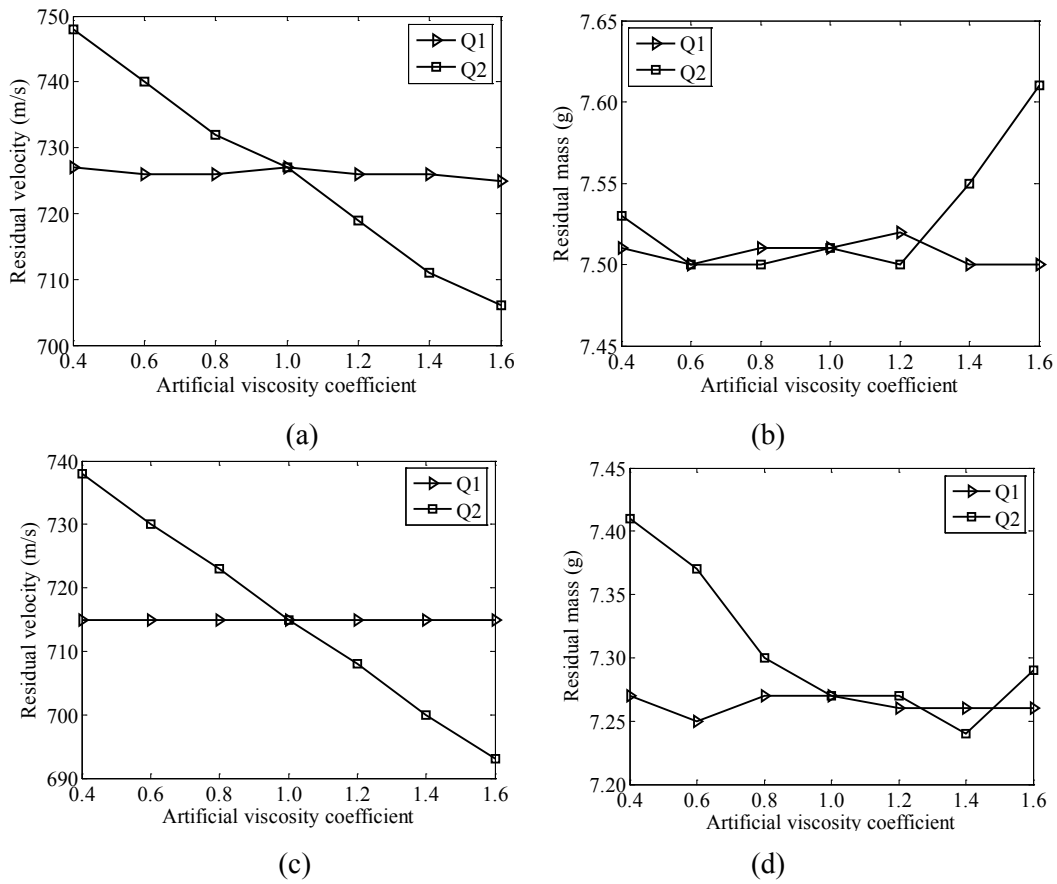
From the results shown in Section 3, it can be seen that there is only slight difference when contacts between different SPH parts are treated with PCM and PAM. A main reason for this is that both the projectile material and the target material at contact interfaces are totally damaged and cannot undergo any shear stress. Besides, the interactions between the projectile and the target are mainly compressive in the impact process due to the mushrooming deformation of the projectile. Hence, the development of spurious shear and tensile stresses at interfaces is insignificant when PAM is used for contact treatment.

#### **4 Analysis of parametric effects**

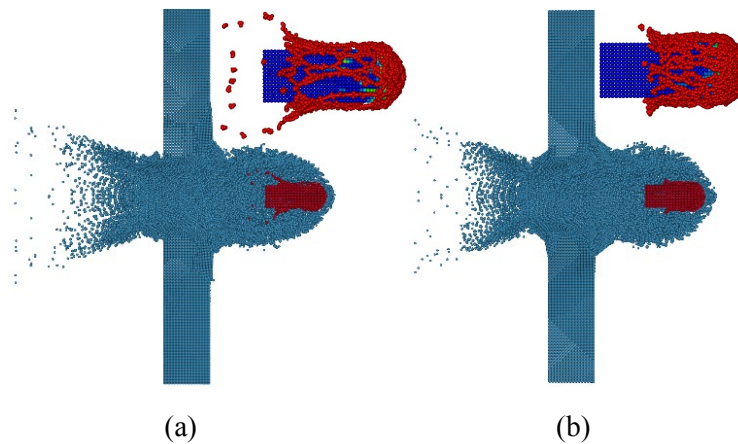
It is known that SPH has some parameters for users to choose to adapt to simulations of various problems. The parameters include the coefficients for artificial viscosity ( $Q_1$  and  $Q_2$ ) and the constant applied to smoothing length (CSLH), as mentioned in Section 2. These parameters may influence simulation results to different extents. In this section, effects of these parameters are investigated for the current problem.

##### **4.1 Effects of artificial viscosity**

The Monaghan type artificial viscosity is used in this work. It contains two parameters, the quadratic coefficient  $Q_1$  and the linear coefficient  $Q_2$ . To assess their effects on simulation results, a series of values around their recommended values (1.0) are used to simulate the impact process. When effects of  $Q_1$  is studied,  $Q_2$  is fixed at 1.0. A similar procedure is used for the study of effects of  $Q_2$ . Figs. 9(a) and 9(c) show the effects of  $Q_1$  and  $Q_2$  on the simulated residual velocity of the projectile. The effects are similar for both SPH with PCM and SPH with PAM. The simulated residual velocity is hardly affected by  $Q_1$ , while it is obviously affected by  $Q_2$ . The reason for this is because the quadratic artificial viscosity term is primarily devised to deal with shocks of high Mach number [Monaghan (2005)], while in the current problem particle velocities are small in comparison with the sound speed. Thus, the effect of artificial viscosity is dominated by the linear artificial viscosity term ( $Q_2$ ). The simulated residual velocity tends to decrease as  $Q_2$  increases, which indicates that the artificial viscosity introduces additional energy dissipation and enhanced strength to materials. The simulated residual mass seems to be insensitive to both  $Q_1$  and  $Q_2$ , as shown in Figs. 9(b) and 9(d). Figs. 10 and 11 show the deformations of the projectile and the target at 60  $\mu\text{s}$  (i.e., the end of simulation) obtained by SPH with PCM and SPH with PAM, respectively. A section view of the whole system and a local view of the projectile are given in each subfigure. When  $Q_2$  ranges from 0.4 to 1.6, the impact process is stably simulated. Simulated deformation modes of targets are similar for different values of  $Q_2$ . However, ejecta at the front face is more distributed, and bulge at the rear face has a larger aspect ratio when a smaller  $Q_2$  is used. Also, with a smaller value of  $Q_2$ , projectile material appears to flow to the projectile tail more freely and fracture more severely. According to the results shown above, we can conclude that the value of the artificial viscosity parameter  $Q_2$  must be carefully selected to obtain accurate simulation results. A relatively simple approach to calibrating the parameter  $Q_2$  is to match the simulated residual velocity of the projectile with the experimental one through adjusting  $Q_2$ , since the residual velocity is sensitive to it and easily measured in high velocity impact processes. According to this approach, the reasonable value of  $Q_2$  can be obtained by linear fitting of the residual velocity results shown in Figs. 9(a) and 9(c). In the case of particle spacing 0.4 mm and CSLH 1.2 used in this section, the best value of  $Q_2$  is found to be 2.3 when PCM is used and 1.9 when PAM is used. Beside the residual velocity, morphological parameters of the deformed target and projectile can be combined to calibrate the parameter  $Q_2$  more reasonably.



**Figure 9:** Effects of artificial viscosity coefficients on residual velocity and mass: (a) Residual velocity for PCM; (b) Residual mass for PCM; (c) Residual velocity for PAM; (d) Residual mass for PAM



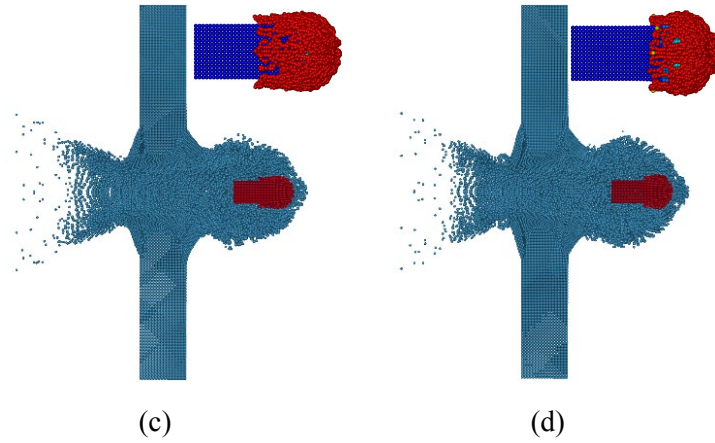


**Figure 10:** Deformations of projectile and target at  $60 \mu\text{s}$  obtained by SPH with PCM: (a)  $Q_2=0.4$ ; (b)  $Q_2=0.8$ ; (c)  $Q_2=1.2$ ; (d)  $Q_2=1.6$

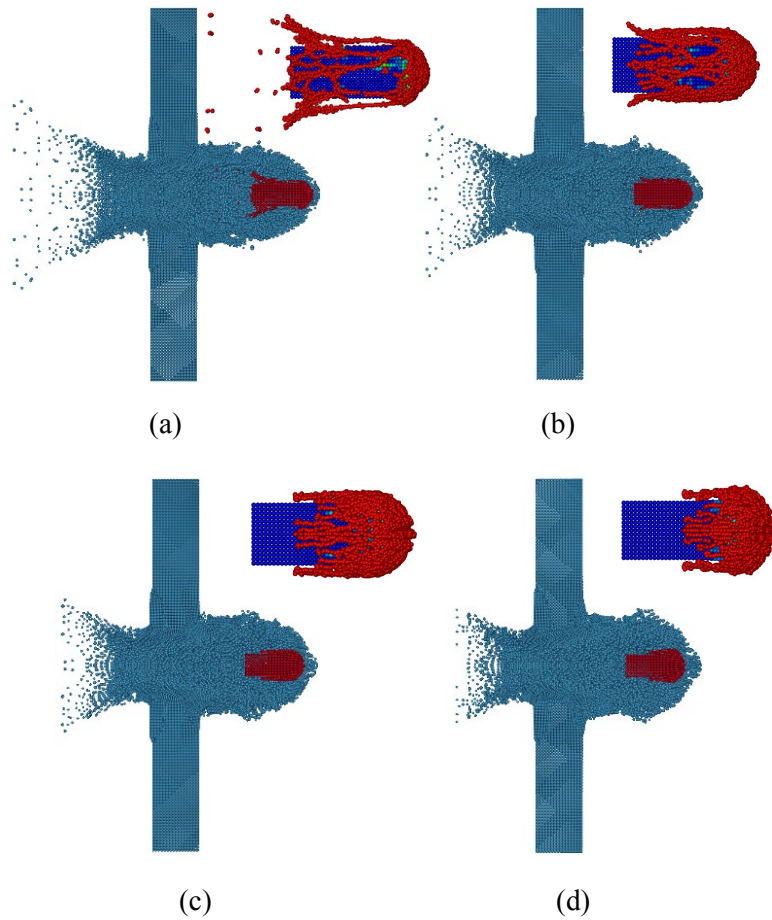


**Figure 11:** Deformations of projectile and target at  $60 \mu\text{s}$  obtained by SPH with PAM: (a)  $Q_2=0.4$ ; (b)  $Q_2=0.8$ ; (c)  $Q_2=1.2$ ; (d)  $Q_2=1.6$

**4.2 Effects of smoothing length**

When particle spacing is given, the constant applied to smoothing length (CSLH) determines the size of smoothing length and consequently the number of neighboring particles. It affects not only accuracy but also efficiency of simulation. To assess its effects on simulation results, a series of values covering the recommended range 1.05-1.3 are used for CSLH to simulate the impact process. Tab. 4 gives the simulated residual velocities and masses of the projectile for SPH with PCM. When CSLH is taken as values less than 1.2, non-physical penetrations occur between the projectile and the target for SPH with PCM (see an example shown in Fig. 12), so the corresponding results are not reported. When CSLH increases from 1.2 to 1.5, both simulated residual velocity and residual mass tend to decrease. One reason for this is that nonlocal effect is enhanced, and strain and damage are less localized when the size of smoothing domain increases with the growth of CSLH. Another reason is that increasing smoothing length leads to larger artificial viscosity due to increased  $\varphi_{ij}$  ( Eq. (12)) for each neighboring particle pair and increased number of neighboring particle pairs. Tab. 5 gives the simulated residual velocities and masses of the projectile for SPH with PAM. The relations of simulated residual velocity and mass to CSLH are similar to those for SPH with PCM. Compared with SPH with PCM, SPH with PAM can use a smaller CSLH to simulate the impact process.

**Table 4:** Residual velocity and residual mass for SPH with PCM using different smoothing lengths

CSLH	Residual velocity (m/s)	Residual mass (g)
1.2	727	7.51
1.3	715	7.38
1.4	709	7.35
1.5	698	7.03

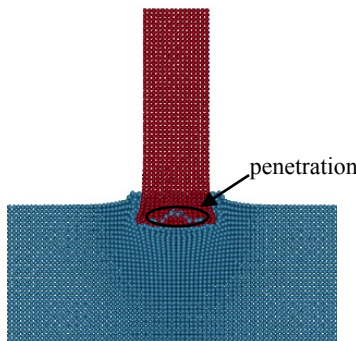


**Figure 12:** Non-physical penetration occurring in the case of using CSLH=1.1 for SPH with PCM

**Table 5:** Residual velocity and residual mass for SPH with PAM using different smoothing lengths

CSLH	Residual velocity (m/s)	Residual mass (g)
1.0	724	7.50
1.1	720	7.35
1.2	715	7.27
1.3	708	7.18
1.4	699	7.04
1.5	693	6.87

Figs. 13 and 14 show deformations of the projectile and the target at 60  $\mu$ s obtained by SPH with PCM and SPH with PAM, respectively, when different smoothing lengths are used. Simulated deformation modes of targets are similar for different smoothing lengths. Conical-shaped ejecta at the front face and expanding bulge at the rear face are observed. With the increase of smoothing length, simulated deformation of the projectile becomes more continuous. In computational efficiency, SPH with PCM is basically the same as SPH with PAM when using the same smoothing length. When CSLH changes from 1.0 to 1.5, computation time used to complete the simulation increases by about 60%. According to the results shown above, smoothing length has some influence on the prediction accuracy of both residual velocity and residual mass, so it should be selected reasonably. Smoothing length in SPH acts as the characteristic length in nonlocal damage theory [Pijaudier-Cabot, ASCE, Bažant et al. (1987)]. It determines the size of the domain where history variables are averaged to introduce nonlocal effects and prevent damage localization. The characteristic length in nonlocal damage theory is considered to be in the order of the maximum size of material inhomogeneities, for example, about 2.7 times the maximum aggregate size for concrete [Bažant and Pijaudier-Cabot (1988)]. Only above such a size, a macroscopic equivalence between a real heterogeneous material and an assumed continuum with damage may be achieved. Thus, from the perspective of averaging history variables to prevent damage localization, the smoothing length in SPH should be the same as the characteristic length of the material and related to the size of material inhomogeneities. For the alumina material considered here, it should be several times grain size, since it is a heterogeneous material composing of grains. This size is comparable to that for the macroscopic equivalence between a real heterogeneous alumina and its assumed continuum. This can be seen from the grain-level analysis of dynamic fragmentation of alumina ceramics performed by Nittur et al. [Nittur, Maiti and Geubelle (2008)], which showed that the representative volume element should have at least 5.8 grains along its width to achieve a convergent macroscopic constitutive response. However, from the perspective of numerical calculation, the smoothing length in SPH should be related to the particle spacing, since it determines the number of neighboring particles used in the particle approximation calculation. If the smoothing length is too large compared with the particle spacing, then there will be too many neighboring particles involved in the particle approximation to ensure an affordable

computational cost. Conversely, if the smoothing length is too small compared with the particle spacing, then there will be too few neighboring particles to obtain a particle approximation of acceptable accuracy. As for an optimum smoothing length, it is physically meaningful to determine it according to the characteristic length of the material. Then, a reasonable particle spacing can be chosen to ensure the accuracy and efficiency of particle approximation according to the determined smoothing length. However, the actual characteristic length of material is unknown in many cases, such as the case of this work. Then one has to compromise to numerically identify an optimum smoothing length with a pre-selected particle spacing. For the current problem, it may be identified by matching experimental and simulated results of residual mass, residual velocity and damage morphology.

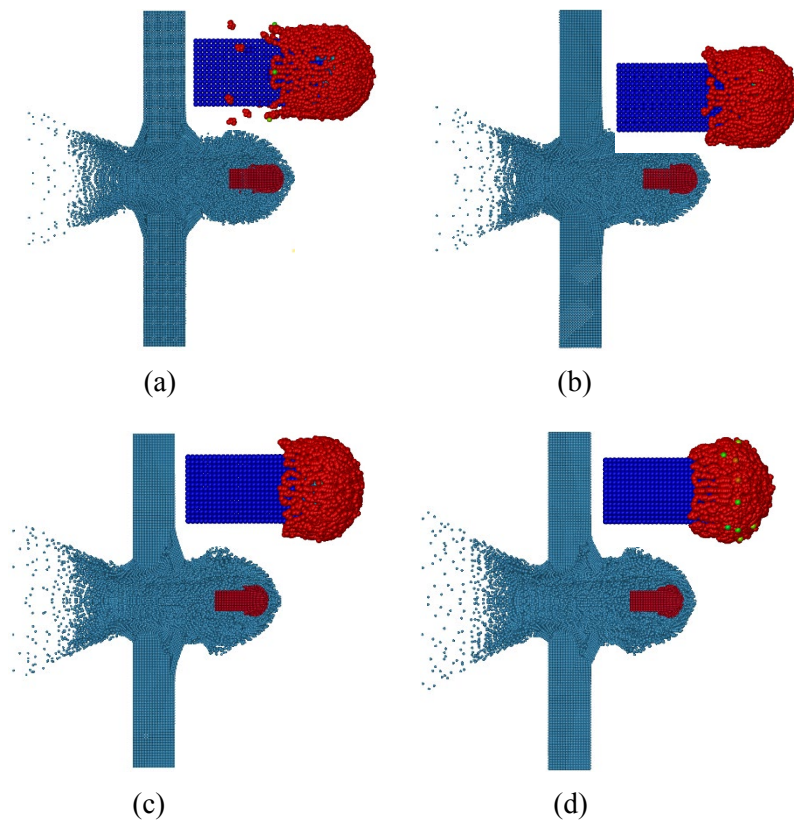


**Figure 13:** Deformations of projectile and target at 60  $\mu$ s obtained by SPH with PCM: (a) CSLH=1.2; (b) CSLH=1.3; (c) CSLH=1.4; (d) CSLH=1.5

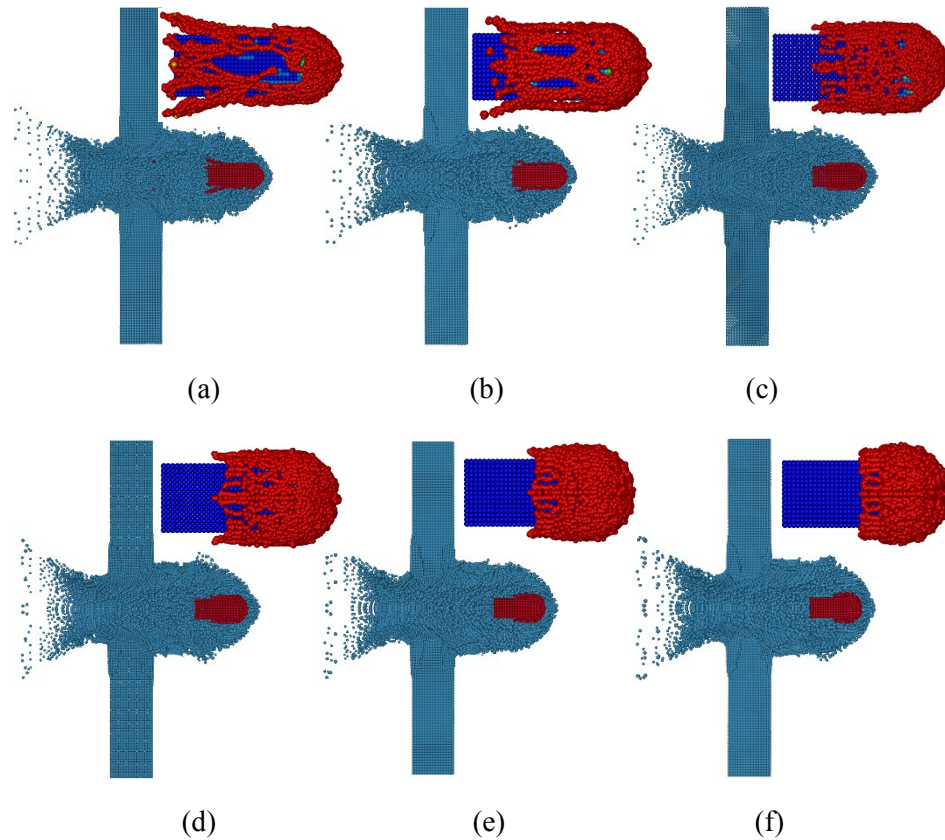


**Figure 14:** Deformations of projectile and target at  $60 \mu\text{s}$  obtained by SPH with PAM: (a) CSLH=1.0; (b) CSLH=1.1; (c) CSLH=1.2; (d) CSLH=1.3; (e) CSLH=1.4; (f) CSLH=1.5

### 5 Approach for reducing particle spacing sensitivity

In Section 3, particle spacing sensitivity is observed. The reason is that the parameter CSLH is fixed at a constant (1.2), and the smoothing length ( $\text{CSLH} \times \text{spacing}$ ) decreases as the particle spacing decreases. Consequently, the nonlocal effect inherently introduced in SPH is reduced, and the strain and damage become more localized, so increased residual velocity and mass of the projectile are obtained with the decrease of particle spacing. To reduce the particle spacing sensitivity, a possible approach is to use an identical smoothing length for different particle spacings. This can be easily achieved by modifying CSLH to keep  $\text{CSLH} \times \text{spacing}$  as a constant. However, when an identical smoothing length is used for different particle spacings, the number of neighboring particles for each particle will increase as particle spacing decreases. Since an artificial viscosity term  $q$  (Eq. (11)) is added for each neighboring particle pair, the total artificial viscosity introduced tends to increase as the number of neighboring particles increases. It is difficult to quantitatively assess the enhancement of artificial viscosity induced by increased neighboring particles. To balance this effect, a direct way is to reduce artificial viscosity coefficients for a smaller particle spacing when using an identical smoothing length for different particle spacings. As seen from the parametric effect analysis in

Section 4, the quadratic artificial viscosity term has insignificant effects on SPH simulation results. Hence, it is only necessary to modify the linear artificial viscosity coefficient  $Q_2$ , while the modification of the quadratic artificial viscosity coefficient  $Q_1$  can be ignored. In this work,  $Q_2$  is modified to balance the artificial viscosities for different particle spacings as follows:

$$Q_2(\Delta) = Q_2(\Delta_0) \Delta / \Delta_0, \tag{35}$$

where  $\Delta_0$  denotes the reference particle spacing, and  $\Delta$  is any other particle spacing to be compared with the reference particle spacing in particle spacing sensitivity test.

Tab. 6 gives the simulated residual velocities and masses using identical smoothing length and balanced artificial viscosity. The simulation results are obtained by SPH with PAM. Identical smoothing length is only used for adjacent particle spacings to avoid a too large CSLH, since an excessive CSLH leads to too many neighboring particles and makes the computation infeasible. As seen in Tab. 6, when identical smoothing length and balanced artificial viscosity are used, the results using particle spacings 0.8 mm and 0.6 mm show only a difference of 2 m/s for residual velocity, which is much less than the corresponding difference (16 m/s, see Tab. 3) observed in the particle spacing sensitivity test of Section 3.1. The differences between the residual velocities for other compared particle spacing pairs, 0.6 mm vs. 0.4 mm and 0.4 mm vs. 0.3 mm, are also significantly reduced. As for residual mass, the average difference for the three compared particle spacing pairs is 0.12 g (1.9% of the experimental result), when identical smoothing length and balanced artificial viscosity are used. It is much less than the corresponding difference (0.31 g, i.e., 4.8% of the experimental result) observed in the particle spacing sensitivity test of Section 3.1. The above results indicate that the particle spacing sensitivity is significantly reduced with the proposed approach.

**Table 6:** Simulated residual velocities and masses using identical smoothing length and equivalent artificial viscosity

Smoothing length (mm) (CSLH×spacing)	Particle spacing (mm)	CSLH	$Q_2$	Residual velocity (m/s)	Residual mass (g)
0.96	0.8	1.20	1.0	676	6.65
0.96	0.6	1.60	0.75	678	6.72
0.72	0.6	1.20	1.0	692	7.23
0.72	0.4	1.80	0.667	697	7.04
0.48	0.4	1.20	1.0	715	7.27
0.48	0.3	1.60	0.75	721	7.37

## 6 Conclusions

SPH models are established to simulate fracture and fragmentation of the projectile and the target during the impact process of an Al<sub>2</sub>O<sub>3</sub> ceramic tile by a blunt tungsten projectile. Two methods including penalty contact method (PCM) and particle approximate method

(PAM) are employed to handle interactions between the projectile and the target. The simulated results are compared with experimental results and other numerical simulation results obtained by fragmentation method and erosion method. Effects of SPH parameters on simulation results are investigated. A simple approach for reducing particle spacing sensitivity is explored. The main conclusions are drawn as follows:

(1) SPH is feasible to capture main features of the impact fragmentation of the target and the projectile with appropriate parameters setting. The formation and movement of ejecta at the target's front face and bulge at its rear face are properly reproduced. The mushrooming deformation and erosion process of the projectile are also reasonably reproduced. The simulated morphologies of the fragmented target and projectile are qualitatively in good agreement with those observed by the experiment.

(2) SPH achieves a good prediction accuracy of the residual velocity of the projectile. The prediction accuracy of residual velocity of SPH is comparable to that of the fragmentation method, while is much better than that of the erosion method. SPH can also achieve an acceptable prediction accuracy of the residual mass of the projectile. Its prediction accuracy of residual mass is much better than that of the fragmentation method and the erosion method. SPH with our residual mass determination method generally overestimates the residual mass of the projectile.

(3) Contact treatments with PCM and PAM induce insignificant differences for SPH simulation of the high velocity impact of the deformable projectile on the ceramic tile. When PCM is used for contact treatment, it is necessary to carefully choose the parameters (SRAD and CSLH) related to contact detection to prevent the problems of non-physical penetration. Thus, it is recommended to use PAM for simulations of high velocity impacts of ceramics for simplicity.

(4) SPH simulation results of residual velocity show some sensitivity to artificial viscosity. The effect of  $Q_2$  is important, while the effect of  $Q_1$  is ignorable. SPH simulation results of residual mass appear to be insensitive to both  $Q_1$  and  $Q_2$ . SPH simulation results of both residual velocity and residual mass show some sensitivity to smoothing length, and tend to decrease as smoothing length increases.

(5) SPH simulation results show some sensitivity to particle spacing when a fixed CSLH is used. It is mainly induced by the coupled effect of varying smoothing length and artificial viscosity resulting from the change of particle spacing. The sensitivity to particle spacing can be effectively reduced by using identical smoothing length and balanced artificial viscosity for different particle spacings. This can be easily achieved by changing CSLH and  $Q_2$ .

**Acknowledgement:** Support from National Natural Science Foundation of China (Grant No. 11862005), Natural Science Foundation of Jiangxi Province of China (Grant No. 20181BAB211012) and Tianjin Natural Science Foundation of China (Grant No. 18JCYBJC88500) is gratefully acknowledged. The third author would also like to acknowledge the support from The Personnel Training Plan for Young and Middle-aged Innovation Talents in Universities in Tianjin of China.

**Conflicts of Interest:** The authors declare that there is no conflict of interests regarding the publication of this paper.

## References

- Anderson, C. E.; Morris, B. L.** (1992): The ballistic performance of confined  $\text{Al}_2\text{O}_3$  ceramic tiles. *International Journal of Impact Engineering*, vol. 12, no. 2, pp. 167-187.
- Bažant, Z. P.; Pijaudier-Cabot, G.** (1988): Nonlocal continuum damage, localization instability and convergence. *Journal of Applied Mechanics*, vol. 55, pp. 287-293.
- Bresciani, L. M.; Manes, A.; Romano, T. A.; Iavarone, P.; Giglio, M.** (2016): Numerical modelling to reproduce fragmentation of a tungsten heavy alloy projectile impacting a ceramic tile: adaptive solid mesh to the SPH technique and the cohesive law. *International Journal of Impact Engineering*, vol. 87, pp. 3-13.
- Camacho, G. T.; Ortiz, M.** (1996): Computational modelling of impact damage in brittle materials. *International Journal of Solids and Structures*, vol. 33, no. 20-22, pp. 2899-2938.
- Campbell, J.; Vignjevic, R.; Libersky, L. D.** (2000): A contact algorithm for smoothed particle hydrodynamics. *Computer Methods in Applied Mechanics and Engineering*, vol. 184, no. 1, pp. 49-65.
- Cleary, P. W.** (1998): Modelling confined multi-material heat and mass flows using SPH. *Applied Mathematical Modelling*, vol. 22, no. 12, pp. 981-993.
- Cleary, P. W.; Prakash, M.; Ha, J.** (2006): Novel applications of smoothed particle hydrodynamics (SPH) in metal forming. *Journal of Materials Processing Technology*, vol. 177, no. (1-3), pp. 41-48.
- Clegg, R. A.; Hayhurst, C. J.** (1999): Numerical modelling of the compressive and tensile response of glass and ceramic under high pressure dynamic loading. *APS Shock Compression of Condensed Matter Meeting Abstracts*.
- Cottrell, M. G.; Yu, J.; Owen, D. R. J.** (2003): The adaptive and erosive numerical modelling of confined boron carbide subjected to large-scale dynamic loadings with element conversion to undeformable meshless particles. *International Journal of Impact Engineering*, vol. 28, no. 9, pp. 1017-1035.
- Cronin, D. S.; Bui, K.; Kaufmann, C.; McIntosh, G.; Berstad, T.** (2003): Implementation and validation of the Johnson-Holmquist ceramic material model in LS-DYNA. *4th European LS-DYNA Users Conference*, vol. 1, pp. 47-60. Ulm, Germany.
- Gingold, R. A.; Monaghan, J. J.** (1977): Smoothed particle hydrodynamics: theory and application to non-spherical stars. *Monthly Notices of the Royal Astronomical Society*, vol. 181, no. 3, pp. 375-389.
- Han, Z. D.; Liu, H. T.; Rajendran, A. M.; Atluri, S. N.** (2006): The applications of meshless local Petrov-Galerkin (MLPG) approaches in high-speed impact, penetration and perforation problems. *Computer Modeling in Engineering & Sciences*, vol. 14, no. 2, pp. 119-128.
- Hedayati, E.; Vahedi, M.** (2017): Numerical investigation of penetration in ceramic/aluminum targets using smoothed particle hydrodynamics method and presenting

a modified analytical model. *Computer Modeling in Engineering & Sciences*, vol. 113, no. 3, pp. 295-323.

**Hogan, J. D.; Farbaniec, L.; Mallick, D.; Domnich, V.; Kuwelkar, K. et al.** (2017): Fragmentation of an advanced ceramic under ballistic impact: mechanisms and microstructure. *International Journal of Impact Engineering*, vol. 102, pp. 47-54.

**Hogan, J. D.; Farbaniec, L.; Shaeffer, M; Ramesh, K. T.** (2015): The effects of microstructure and confinement on the compressive fragmentation of an advanced ceramic. *Journal of the American Ceramic Society*, vol. 98, no. 3, pp. 902-912.

**Holmquist, T. J.; Templeton, D. W.; Bishnoi, K. D.** (2001): Constitutive modeling of aluminum nitride for large strain, high-strain rate, and high-pressure applications. *International Journal of Impact Engineering*, vol. 25, no. 3, pp. 211-231.

**Johnson, G. R.; Holmquist, T. J.** (1994): An improved computational constitutive model for brittle materials. *AIP Conference Proceedings*, vol. 309, pp. 981-984.

**Johnson, G. R.; Stryk, R. A.; Beissel, S. R.** (1996): SPH for high velocity impact computations. *Computer Methods in Applied Mechanics and Engineering*, vol. 139, pp. 347-373.

**Kane, A.; Børvik, T.; Hopperstad, O. S.; Langseth, M.** (2009): Finite element analysis of plugging failure in steel plate struck by blunt projectile. *Journal of Applied Mechanics*, vol. 76, pp. 051302.

**Krell, A.; Strassburger, E.** (2014): Order of influences on the ballistic resistance of armor ceramics and single crystals. *Materials Science and Engineering: A*, vol. 597, pp. 422-430.

**Levy, S.; Molinari, J. F.** (2010): Dynamic fragmentation of ceramics, signature of defects and scaling of fragment sizes. *Journal of the Mechanics and Physics of Solids*, vol. 58, no. 1, pp. 12-26.

**Liu, G. R.; Liu, M. B.** (2003): *Smoothed Particle Hydrodynamics: A Meshfree Particle Method*. World Scientific, Singapore.

**Liu, M. B.; Liu, G. R.** (2010): Smoothed particle hydrodynamics (SPH): an overview and recent developments. *Archives of Computational Methods in Engineering*, vol. 17, no. 1, pp. 25-76.

**Liu, M. B.; Liu, G. R.; Zong, Z.; Lam, K. Y.** (2003): Computer simulation of high explosive explosion using smoothed particle hydrodynamics methodology. *Computers & Fluids*, vol. 32, no. 3, pp. 305-322.

**Liu, M. B.; Xie, W. P.; Liu, G. R.** (2005): Modeling incompressible flows using a finite particle method. *Applied Mathematical Modelling*, vol. 29, no. 12, pp. 1252-1270.

**Livermore Software Technology Corporation (LSTC)** (2014a): LS-DYNA Theory Manual.

**Livermore Software Technology Corporation (LSTC)** (2014b): LS-DYNA Keywords User's Manual.

- Mao, Z.; Liu, G. R.; Dong, X.** (2017): A comprehensive study on the parameters setting in smoothed particle hydrodynamics (SPH) method applied to hydrodynamics problems. *Computers and Geotechnics*, vol. 92, pp. 77-95.
- Michel, Y.; Chevalier, J. M.; Durin, C.; Espinosa, C.; Malaise, F. et al.** (2006): Hypervelocity impacts on thin brittle targets: experimental data and SPH simulations. *International Journal of Impact Engineering*, vol. 33, no. 1, pp. 441-451.
- Monaghan, J. J.** (1994): Simulating free surface flows with SPH. *Journal of Computational Physics*, vol. 110, pp. 399-406.
- Monaghan, J. J.** (2005): Smoothed particle hydrodynamics. *Reports on Progress in Physics*, vol. 68, pp. 1703-1759.
- Nemat-Nasser, S.; Sarva, S.; Isaacs, J. B.; Lischer, D. W.** (2002): Novel ideas in multi-functional ceramic design. *Ceramic Transactions*, vol. 134, pp. 511-525.
- Nittur, P. G.; Maiti, S.; Geubelle, P. H.** (2008): Grain-level analysis of dynamic fragmentation of ceramics under multi-axial compression. *Journal of the Mechanics and Physics of Solids*, vol. 56, no. 3, pp. 993-1017.
- Parker, R.** (1990): Failure phenomenology of confined ceramic targets and impacting rods. *International Journal of Impact Engineering*, vol. 9, no. 3, pp. 263-27.
- Pijaudier-Cabot, G.; ASCE, S. M.; Bažant, Z. P.; ASCE, F.** (1987): Nonlocal damage theory. *Journal of Engineering Mechanics*, vol. 113, no. 10, pp. 1512-1533.
- Rabczuk, T.; Eibl, J.** (2003): Simulation of high velocity concrete fragmentation using SPH/MLSPH. *International Journal for Numerical Methods in Engineering*, vol. 56, no. 10, pp.1421-1444.
- Rahaman, M. M.; Pathak, A; Roy, D.** (2018): A thermo-visco-plastic damage model and SPH simulations of plugging failure. *Mechanics of Advanced Materials and Structures*, vol. 25, pp. 1374-1382.
- Seo, S; Min, O.** (2006): Axisymmetric SPH simulation of elasto-plastic contact in the low velocity impact. *Computer Physics Communications*, vol. 175, no. 9, pp. 583-603.
- Seo, S; Min, O.; Lee, J.** (2008): Application of an improved contact algorithm for penetration analysis in SPH. *International Journal of Impact Engineering*, vol. 35, no. 6, pp. 578-588.
- Shockey, D. A.; Marchand, A. H.; Skaggs, S. R.; Cort, G. E.; Burkett, M. W. et al.** (2018): Second-order symmetric smoothed particle hydrodynamics method for transient heat conduction problems with initial discontinuity. *Processes*, vol. 6, no. 11, 215.
- Strassburger, E.; Hunzinger, M.; Parimal, P.; McCauley, J. W.** (2013): Analysis of the fragmentation of AlON and spinel under ballistic impact. *Journal of Applied Mechanics*, vol. 80, 031807.
- Xiao, Y. H.; Dong, H. H.** (2017): Studying normal and oblique perforation of steel plates with SPH simulations. *International Journal of Applied Mechanics*, vol. 9, no. 6, 1750091.

**Xu, J. X.; Wang, J.** (2014): Interaction methods for the SPH parts (multiphase flows, solid bodies) in LS-DYNA. *13th International LS-DYNA Users' Conference*. Detroit, USA.

**Yang, G.; Liu, R. Q.; Hu, D. A.; Han, X.** (2016): Simulation of one dimension shock initiation of condensed explosive by SPH method. *Engineering Computations*, vol. 33, no. 2, pp. 528-542.

**Zhang, G. M.; Batra, R. C.** (2004): Modified smoothed particle hydrodynamics method and its application to transient problems. *Computational Mechanics*, vol. 34, no. 2, pp. 137-146.

**Zhang, G. M.; Batra, R. C.** (2009): Symmetric smoothed particle hydrodynamics (SSPH) method and its application to elastic problems. *Computational Mechanics*, vol. 43, no. 3, pp. 321-340.

**Zhang, Z. L.; Liu, M. B.** (2017): Smoothed particle hydrodynamics with kernel gradient correction for modeling high velocity impact in two- and three-dimensional spaces. *Engineering Analysis with Boundary Elements*, vol. 83, pp. 141-157.